Received: 9 July 2020 | Revised: 28 September 2020 | Accepted: 28 September 2020

DOI: 10.1002/eng2.12311

RESEARCH ARTICLE

WILEY

High-resolution depth measurements in digital microscopic surgery

Sebastian Babilon | **Paul Myland** | **Lucas Schlestein** | **Julian Klabes** | **Tran Quoc Khanh**

Laboratory of Lighting Technology, Technical University of Darmstadt, Darmstadt, Germany

Correspondence
Sebastian Babilon, Laboratory of Lighting Technology, Technical University of Darmstadt, Hochschulstr. 4a, 64289 Darmstadt, Germany.
Email: babilon@lichttechnik.tu-darmstadt.de

Abstract

Fully digital microscopes are becoming more and more common in surgical applications. In addition to high-resolution stereoscopic images of the operating field, which can be transmitted over long distances or stored directly, these systems offer further potentials by supporting the surgical workflow based on their fully digital image processing chain. For example, the image display can be adapted to the respective surgical scenario by adaptive color reproduction optimization or image overlays with additional information, such as the tissue topology. Knowledge of this topology can be used for computer-assisted or augmented-reality-guided microsurgical treatments and enables additional features such as spatially resolved spectral reconstruction of surface reflectance. In this work, a new method for high-resolution depth measurements in digital microsurgical applications is proposed, which is based on the principle of laser triangulation. Part of this method is a sensor data fusion procedure to properly match the laser scanner and camera data. In this context, a strategy based on radial basis function interpolation techniques is presented to handle missing or corrupt data, which, due to the measuring principle, can occur on steep edges and through occlusion. The proposed method is used for the acquisition of high-resolution depth profiles of various organic tissue samples, proving the feasibility of the proposed concept as a supporting technology in a digital microsurgical workflow.

KEYWORDS

AR-guided microsurgical treatments, depth measurements, digital image processing, laser sensor, medical imaging, tissue topology

1 | INTRODUCTION

The use of surgical microscopes has become the gold standard for many ophthalmic, otorhinolaryngological, and neurosurgical procedures.[1-4] In addition to conventional optical surgical microscopes, fully digital solutions are more and more common in clinical practice. Besides offering high-resolution and even stereoscopic vision of the operative field, most of

these systems are intended to provide additional benefit by supporting the surgical workflow based on their completely digital image processing chain. Potential advantages of digital over conventional optical systems comprise, for example, the in situ visualization of preoperative image data (acquired, eg, from tomographic scanning procedures), the overlay of the surgeon's view with signals from external video sources (eg, from an additional endoscope), and the possibility of collaborative viewing and improved surgical assistance by synchronizing the surgeon's exact view of the operative field to external monitors.

Various approaches to further explore the benefits of digital microscopes for surgical applications are reported in the literature, most of which are related to the development of new and dedicated image processing algorithms. Gard et al,[5] for example, proposed a new method of precise distance and contour measurements of patient specific anatomy without external hardware by tracking a marked spherical instrument tip in the stereoscopic image pair provided by a digital surgical microscope. They showed that by applying a self-updating template-matching algorithm sufficiently accurate distance measurements in the submillimeter regime could be achieved depending on the zoom level and the microscope's depth-of-field. In combination with stereo triangulation, their method enabled the reconstruction of instrument tip trajectories that could eventually be used as precisely registered augmented-reality (AR) overlays projected into the surgeon's field of view.

Based on a similar approach, the MultiARC project[6] aims to develop an interactive and multimodal AR system for computer-assisted ear, nose, and throat (ENT) microsurgery. This system is intended to allow for interactive remote surgical assistance including live annotations, three-dimensional point-to-point distance measurements, and the overlaying visualization of preoperatively acquired patient's data (eg, from magnetic resonance imaging). Potential benefits of providing additional AR information as an integrative part of the digital microscope's image processing pipeline are discussed by Aschke et al[7] in the context of neurosurgical treatments. A more general overview can be found in Khor et al,[8] who besides emphasizing the huge potential of such digital surgical environments also elaborate on their current practical limitations.

Another aspect recently discussed in the context of AR-supported microsurgery is the feasibility of automated tissue recognition based on hyperspectral imaging (HSI, see Lu and Fei[9] for a review on HSI in medical applications). As a first proof-of-concept, Wisotzky et al[10,11] developed an HSI setup to noninvasively analyze the optical characteristics of in vivo tissue samples encountered during ENT microsurgery in order to explore the suitability of this approach. They equipped a digital surgical microscope with an additional filter wheel which was placed in front of the white-light LED illumination unit holding 16 different narrow bandpass filters. By synchronizing the rotation of the filter wheel and, therefore, the spectral changes of the illumination of the surgical field with the image capturing frame rate of the microscope, they were able to capture the spectral reflection behavior of various tissue structures in the visible range from 400 to 700 nm. The evaluation of the collected data showed that even for tissue samples which are not or hardly distinguishable for the human eye, the analysis in the 16-dimensional wavelength domain lead to clearly different, individually unique trends in the samples' reflection characteristics allowing for a robust tissue differentiation.

One of the downsides of this method as discussed by Wisotzky et al is the existing time misalignment which is caused by the rather slow rotation of the filter wheel making its current implementation inapplicable for clinical routine. In a further paper, Wisotzky et al[12] therefore proposed a novel HSI approach replacing the filter wheel by two hyperspectral snapshot cameras covering the visible and near-infrared range from 460 to 980 nm. This new setup allowed for acquiring the complete hyperspectral data set in a single shot making it more suitable for clinical application. However, single snapshot HSI always comes with the cost of significantly reduced spatial resolution due to the large filter arrays (here: 4×4 and 5×5, respectively) applied to the camera sensor's surface. In addition, both the filter wheel and the camera-based approach require very expensive and complex components to be additionally mounted to the surgical microscope, considerably increasing engineering effort and production costs.

For these reasons, we worked on a new HSI approach for estimating the spectral reflectance characteristics of organic tissue samples without the need for expensive hardware supplements. The theoretical framework and first results of this approach have recently been published elsewhere.[13] In principle, the idea is to combine the light emission of various narrow-banded monochromatic and phosphor-converted white LEDs creating the multichannel illumination unit of the digital microscope with the imaging capabilities of its standard three-channel RGB camera system. During data acquisition, the tissue sample under inspection is illuminated by flashing the individual LED channels one after the other. At the same time, the image capturing has to be synchronized to this illumination sequence, which artificially increases the dimensionality of the output data without the need of additional hardware or costly equipment. As a result, one obtains $n \times 3$ monochromatic images of the same tissue sample, where n denotes the number of different LED channels, which can subsequently be used as input for applying a Wiener-filter estimation approach[14-18] to reconstruct the tissue's

spectral reflectance characteristics in the visible regime. Note that a similar spectral reconstruction procedure is proposed as part of the MultiARC project discussed above.

Once the reflectance characteristics are known, it was found that significantly enhanced color correction can be achieved during image processing.[13] Leading to improved color reproduction properties, such an enhancement is considered to be beneficial for the success of video-assisted surgeries, where, in general, different kinds of tissues and critical structures must be distinguished by the surgeon not just through their textures but also through their colors. In addition, promising results were obtained with regard to the premises of automated tissue recognition based on previous reflectance estimation.

However, as shown in our recent paper, for the required absolutely correct intensity scaling, the underlying Wiener-filter estimation technique demands the exact knowledge of the measurement geometry, which is determined by the distance and angle of the tissue surface with respect to the illumination and image capturing modules of the surgical microscope. A corresponding pixel-position-dependent scaling factor $\delta^{(i,j)}$ was therefore introduced and determined for the reported measurements by previous calibration using a standard reflectance target at a fixed geometry. However, such a calibration procedure to be conducted in advance of a surgery is not really convenient in practice and must be reperformed every time the microscope head is moved to another position.

Basically, this scaling factor can also be determined from the known pixel position (i,j) of the point-of-interest (POI) in the projected x-y-plane, for which the reflectance spectra should be estimated, and an additional depth measurement to determine the absolute distance value ρ between the POI and its corresponding location on the imaging sensor along the z-axis. From these geometric measurements, the known position of the multichannel LED illuminant in relation to the image capturing module, and an initial one-time calibration during the manufacturing process, the absolute spectral power distribution (SPD) in terms of the spectral flux received by the tissue surface at the POI position can be derived for each given LED channel. Once the individual SPDs at the POI position are known, they can be used as input in the Wiener-filter matrix (see previous work[13] for corresponding equations) to properly estimate the spectral surface reflectance at the POI on an absolute scale.

Even though the actual calculations and the algorithmic implementation are straightforward, the challenging task is to accurately perform the depth measurements, not only for tissue recognition but also with regard to AR-guidance and in situ navigation.[19] In preparation of the current work, it was found in a pretest adopting the Wiener-filter approach that uncertainties of up to 3 mm in the depth measurements result in average deviations of the reconstructed reflectance spectra from the ground truth of about 2.5%. This empirical estimate is based on micron-precise systematic variations of the absolute distance value ρ for known specimens without readjusting the scaling factor $\delta^{(i,j)}$. Hence, with regard to the idea of automated tissue recognition based on reflectance estimation, a depth accuracy of less than ± 0.3 mm would be favorable to keep the expected deviations from the ground truth due to systematic depth measurement inaccuracies below 1%.

Since modern digital surgical microscopes usually provide stereoscopic imaging, trying to extract depth information directly from the corresponding disparity mapping seems to be quite obvious. Based on stereo computer vision theory,[20] the accuracy in depth estimation can be approximated by

$$|\Delta\rho| = \frac{Z^2}{fB}\Delta d, \tag{1}$$

where f is the focal length, B is the baseline distance of the stereo camera configuration, and Δd is the error of the disparity calculation between the left and right image. This also called correspondence accuracy describes the expected error caused by an incorrect matching of both images at the POI location and depends on image noise, scene texture, and other scene properties such as occlusions and non-Lambertian surfaces,[21] the used matching algorithm as well as on the resolution and pixel size of the camera sensors.[20]

In benchmark tests for the performance evaluation of different matching algorithms, such as for example the Middlebury Stereo Evaluation,[22] average disparity errors of 2 to 3.5 pixels can be found for the best performing algorithms under controlled experimental conditions. Assuming further a typical focal length of surgical microscopes ranging between 45 and 80 mm, a baseline distance of the (virtual) stereo camera configuration ranging from 16 to 22 mm, and a pixel size of the camera sensors of 6 to 8 μm,[6] the accuracy in depth estimation under optimal conditions obtain from disparity mapping is expected to be of the order of ± 0.6 to ± 1.6 mm for an assumed working distance of 250 mm.

With regard to the indicated depth resolution of ± 0.3 mm required for accurate in situ reflectance reconstruction, a direct depth estimation from stereoscopic imaging of currently available surgical microscopes seems to be inexpedient.

Hence, a new approach for high-resolution in situ depth measurements based on laser triangulation was developed by the authors and will be presented in the following. Although laser triangulation is an established method in industrial production processing and has already been tested in various other biomedical applications,[23-25] the presented work, to the authors' best knowledge, is the first to make use of this concept for achieving highly accurate depth measurements in microsurgical treatments.

The structure of this article is organized as follows. Section 2 starts with a short discussion of the experimental setup and the measurement protocol used for data acquisition. In Section 3, the applied strategies for accuracy estimation, sensor data fusion, and data visualization will be presented. Based on these preconditions, first depth profiling results for various organic tissue samples will be reported in order to qualitatively evaluate the performance of the proposed method. Finally, a short summary of the key findings of this work as well as an outlook on future research intentions will be given in Section 4.

2 | EXPERIMENTAL SETUP AND MEASUREMENT PROTOCOL

High-precision laser-triangulation modules are common components of modern coordinate measuring machines in various industrial production processes. They are typically used for quality control, safety, level measurements, and positioning applications. Being solely based on trigonometry, they are relatively simple and cost-efficient measuring tools that allow for robust and accurate distance measurements well into the micrometer range. Due to this accuracy and outstanding depth resolution, laser triangulation is used in this work to determine the pixel-dependent scaling factor $\delta^{(i,j)}$ required for the microsurgical application sketched in the introduction.

Its basic principle is shown in Figure 1. A laser emitter, which consists of a laser diode of a certain wavelength supplemented with dedicated transmitting optics components, is used to project a light spot onto the surface of an object whose distance ρ should be measured. The scattered light from the object's surface is collected by the receiving optics and focused on a position sensitive detector (PSD; eg, a CCD sensor). If a change $\Delta\rho$ in the distance between the laser diode and the object's surface occurs, the angle α under which the scattered light is received by the PSD changes accordingly, leading to a position shift $\Delta\nu$ of the focused image of the light spot on the detector's surface. As a result of this relationship, the PSD can be calibrated such that absolute measures of the distance ρ between the laser diode and the surface of the object become feasible.

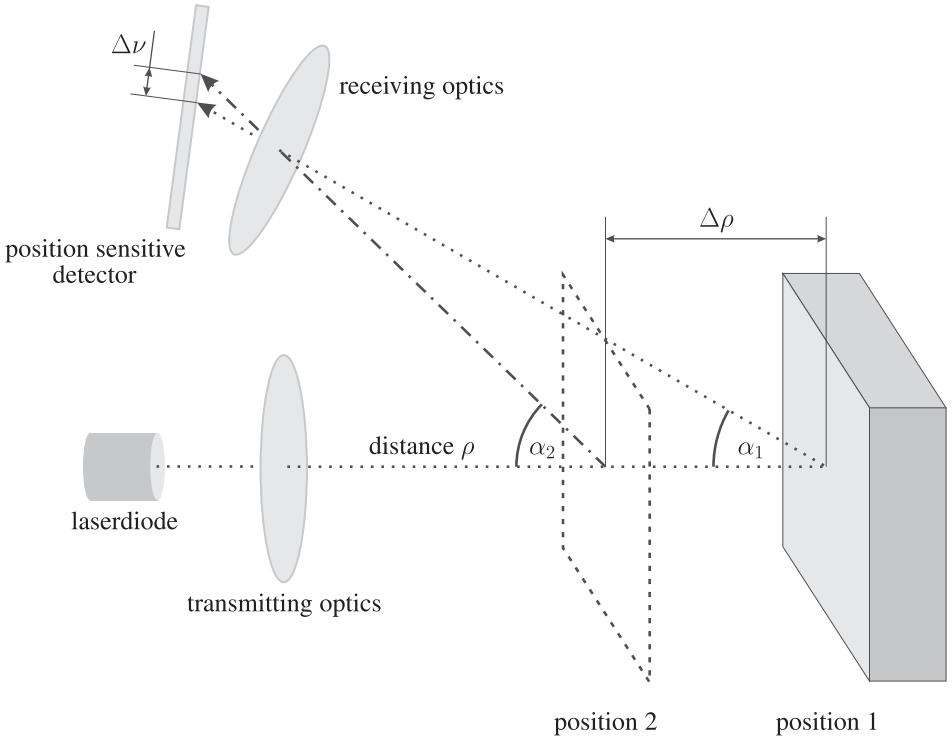

FIGURE 1 Illustration of the laser-triangulation principle. Based on an initial distance calibration, it is possible to determine the corresponding distance ρ between the light emitting laser diode and the reflecting object for each position of the imaged laser spot on the detector's surface in the receiving unit

In order to suppress disturbances caused by the ambient light, the receiving unit is usually equipped with an additional spectral band-pass filter, which is optimized to match the specific wavelength of the laser diode. Other factors that may reduce the accuracy of the distance measurements are, for example, unfavorable surface characteristics, distance-dependent laser spot enlargement, out-of-focus measurements, and optical aberrations such as coma, astigmatism, or spherical errors of the lens systems. With regard to the intended microsurgical application, it is very important to be aware of these error sources and a careful characterization of the final experimental setup must therefore be performed on a dedicated reference target to obtain an estimate of the overall depth measurement accuracy.

For the experimental test setup used in this work, two different laser-triangulation modules with similar specifications but different wavelengths were at our disposal: A red-emitting Micro-Epsilon scanCONTROL 2900-100 with 658 nm wavelength and a blue-emitting Micro-Epsilon scanCONTROL 2900-100/BL with 405 nm wavelength. Both devices are Class 2M ($\leq$8 mW) laser profile scanners, that is, instead of using a single light spot, as shown in Figure 1, they project a complete line segment comprising 1280 individual measuring points onto the object's surface, which will be denoted as the x-axis in the following. According to the corresponding data sheet,[26] they both offer a reference depth resolution of 12 mm within the identical measurement range (working distance) from 190 to 290 mm along the z-axis and the same maximum measurement frequency of 300 Hz. However, pretests with both devices revealed that the blue-emitting laser module is better suited for profiling organic tissue than its red-emitting equivalent, which, compared with the former, suffered from too much failed measurements when being applied to scan various organic test samples. The remaining part of this article should therefore consider the blue-emitting results only.

For a complete scan of an arbitrary object, the scanning device must be moved along the y-axis at a constant velocity v. Figure 2 shows the corresponding experimental setup. As can be seen, the laser scanner and an additional industrial GigE camera are mounted to the carriage of a linear motion system driven by a stepper motor. The linear motion system is held by a stable aluminum profile fixture and oriented such that both scanner and the camera are facing perpendicularly downward to the bottom plate, where the test objects are placed for scanning. Care must be taken to ensure an almost vibration-free attachment. In this setup, the camera, which is a monochrome IDS UI-5490SE-M-GL Rev.2,[27] is intended to simulate the digital imaging of a surgical microscope in order to address the question of how the output of both systems can efficiently be combined in future applications.

The dimensions of the aluminum profile fixture (cf Figure 2) as well as the camera lens ($f = 12$ mm) were chosen to match the measurement range and scanning width of the laser-triangulation module. The stepper motor is used in half step mode to achieve a smooth and even running behavior.[28,29] A relatively low measurement frequency of 50 Hz is chosen as a trade-off between a moderate scanning velocity to reduce vibrations and the total time required for a single scan. The corresponding scanning velocity was adjusted such that an approximately equal resolution in x- and y-direction can be achieved. As a result, an average velocity of (4.153$\pm$ 0.002) mm s^{-1} is obtained, which was determined empirically from repeated measurements ($n = 100$). This gives a resolution along the y-axis of (83.1 $\pm$ 4.2) µm, while the resolution

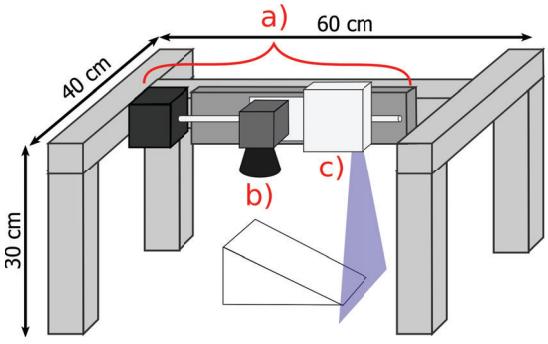

(A) Schematic illustration of the experimental setup including its dimensions

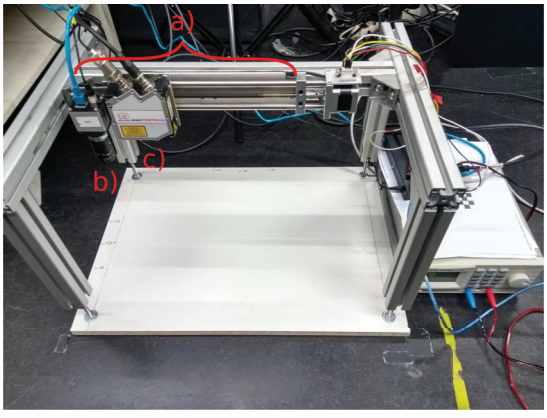

(B) Picture of the experimental setup as it can be found in the laboratory

FIGURE 2 Experimental setup as a first proof-of-concept for high-resolution depth profiling of organic tissue samples based on laser triangulation. Its main parts are, a), the linear motion axis, b), a digital camera system to simulate the imaging workflow of a surgical microscope, and c), the laser-triangulation profile scanner

in x-direction depends on the distance between laser scanner and test object and ranges from approximately 81 μm (for objects with a height of 4 cm) to 94 μm (on the level of the bottom plate). Hence, it can be concluded that the proposed experimental setup allows for high-resolution measurements with sufficiently small uncertainties to generate, as a first proof-of-concept, diagnostically conclusive depth profiles of organic tissue samples with regard to the requirements defined in the introduction.

The corresponding measurement protocol is conceived as follows. After the test object/tissue sample has been centered on the bottom plate, the carriage of the linear motion axis, with both camera and laser scanner being attached to it, is moved from one end of the axis to the other at the given constant scanning velocity. The actual data acquisition starts 1 second after the movement has been initiated and terminates 1 second before the end position is reached in order to exclude the phases of nonlinear motor acceleration and deceleration. During the phase of constant movement, measurements from the laser profile scanner are read every 20 milliseconds, which complies with the desired 50 Hz measurement frequency, so that a total number of approximately 1500×1280 measurements are performed on the tissue sample resulting in a high-resolution depth profile of this test object. After the depth scanning is finished, the carriage is moved backward until the camera and the center of the bottom plate are aligned to ensure the largest possible overlap between the measurement range of the laser scanner and the camera's field of view for a subsequent sensor data fusion (see Section 3.2). Once this specific position is reached, an image of the test object is captured at a resolution of 3840×2748 pixels. Afterward, the carriage is eventually moved back to its initial position and the whole setup is ready for the next acquisition run. In total, it takes approximately 46.5 seconds to complete a single scan.

3 | SCANNING CHARACTERIZATION AND DEPTH MEASUREMENT RESULTS

Based on the description of the experimental setup and the measurement protocol given in the previous section, the following parts are intended to address the issues of data acquisition, error estimation, and data processing. In Section 3.1, the overall depth measurement accuracy along the z-direction should be evaluated. For this purpose, a dedicated reference target was used as a known test sample from which an error estimate is obtained by comparing nominal and measured values by means of residual analysis. This serves as an indicator whether the proposed triangulation method could meet the required depth resolution to be applicable for accurate in situ reflectance estimation as discussed in the Introduction of this article. In Section 3.2, an efficient method of sensor data fusion is presented for matching both laser scanner and camera data as well as for visualizing the generated depth profiles in a genuine workflow. Finally, in Section 3.3, measurement results and acquired depth profiles of two different organic tissue samples are reported as a first proof-of-concept of the proposed method.

3.1 | Depth measurements on reference target

In order to determine the overall error in the depth measurements of the current experimental setup, a dedicated reference target was designed and manufactured accordingly for system characterization. Its form and dimensions are shown in Figure 3. As can be seen, a wedge-shaped reference target was chosen. It is made of purely white polyethylene material with excellently diffuse reflection properties and a nominal production tolerance of ±50 μm. The shape of the reference target is intended to simulate a well-defined surface gradient giving a more realistic estimate of the application-related

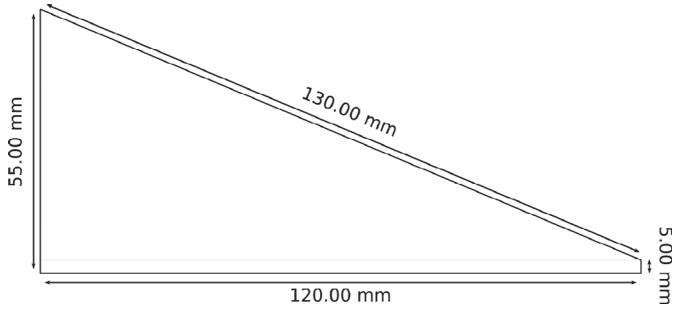

FIGURE 3 Reference target used to determine the overall depth measurement accuracy of the proposed laser-triangulation method. The wedge-shape was chosen to imitate a well-defined surface gradient enabling a more realistic estimation of the application-related measurement errors

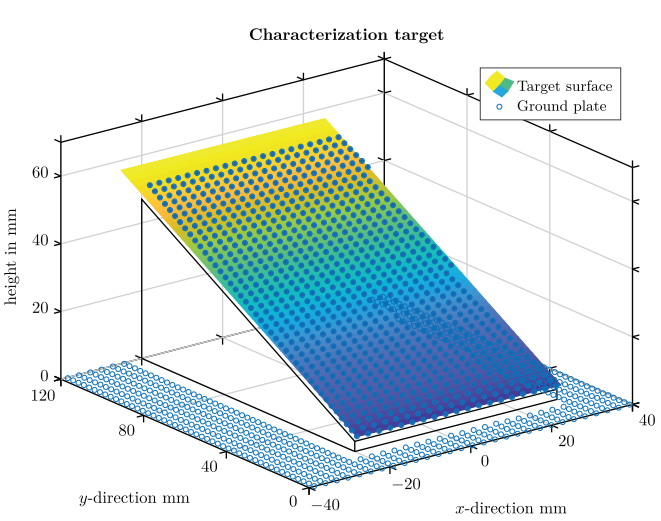

(A) Measured data points and plane fit to approximate the reference target's surface. The number of depicted data points was reduced by a factor of 30 for illustration purposes.

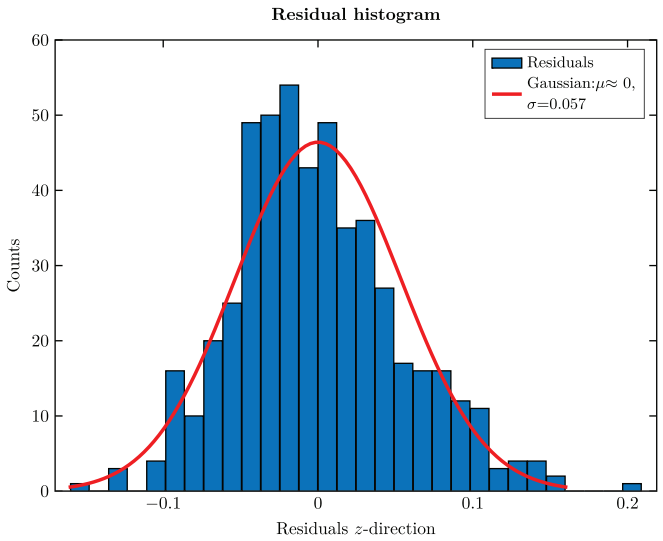

(B) Analysis of the residuals between measured data points and fitted plane model. Twice the standard deviation was used for an estimate of the depth measurement accuracy.

FIGURE 4 Results of the laser-triangulation depth measurements performed on the wedge-shaped reference target. For convenience, a rescaling was applied to transform the z-axis from a distance measure to a height scale (left). Based on the residual analysis (right), an estimate of ± 104 μm is found for the overall depth measurement accuracy

measurement errors. In general, the measurement uncertainty in z-direction also depends on the uncertainties observed for the other directions. In the current setup, mainly the deviations along the y-axis are crucial for the overall depth measurement accuracy because of the respective carriage movement and must therefore be implicated by using a nonflat, gradient-showing reference target, like the one presented here, for the characterization process.

Before the actual characterization started, a baseline measurement had been performed first in order to account for measurement noise and flatness imperfections of the bottom plate and/or the underground. This baseline was then used to correct the actual measurement of the reference target, for which the protocol described in Section 2 was used.

Figure 4A depicts the results of the laser-triangulation depth measurements performed on the wedge-shaped reference target. Rescaling was applied to transform the z-axis from a distance measure to height scale. As can be seen, a plane was fitted to the data points to approximate the reference target's surface. The error estimation was then performed based on the corresponding residuals shown in Figure 4B. Here, twice the standard deviation was chosen giving an estimate of the overall depth measurement accuracy of ± 104 μm.

Compared with the initially formulated requirements, the laser-triangulation method consequently provides a sufficiently accurate depth profiling and distance measurement, which particularly outperforms depth estimation based on stereo vision. Even when considering the full range of the residuals plotted in Figure 4B, which goes up to 205 μm, the required depth resolution of ± 0.3 mm is still met.

3.2 | Sensor data fusion and visualization

Given that the proposed laser-triangulation method clearly complies with the requirements for distance measurement and depth resolution, the next step is to perform the sensor data fusion in order to match the laser scanner and camera data. Since the measurement geometry is always fixed and given by the experimental setup shown in Figure 2, an initial one-time calibration is sufficient. For the sake of efficiency, a standard object recognition approach can be applied to determine the corresponding transformation from the coordinate system of the laser scanner to the coordinate system of the camera.

Assuming affinity between both coordinate systems,[30] this transformation basically consists of a translation, dilation, and rotation, which can be summarized by a single matrix $\mathbf{T}_{\text{affine}}$ projecting data points from one coordinate system into the other, that is,

$$\mathbf{x}_{\text{camera}} = \mathbf{T}_{\text{affine}}\mathbf{x}_{\text{laser}}. \tag{2}$$

In order to determine this projection matrix, a simple cuboid calibration target was used. It is made of black polyethylene and its dimensions read 27.4 mm × 19.6 mm × 2.5 mm. This calibration target was again centered on the bottom plate and the scanning and measurement protocol as described in Section 2 was initiated. The collected profile data of the laser scanner were then transformed to an eight-bit gray-scale image so that an object recognition algorithm can be applied. In Figure 5A and Figure 5B, the resulting "images" of the calibration target as obtained from the laser scanner and camera output are shown and compared with each other.

Next, an adaptive thresholding algorithm[31,32] is applied to transform both images of the calibration target into binary representations that subsequently allow for a straightforward, accurate edge and corner detection of its contours. This is performed by using the OpenCV implementation of the border following algorithm of Suzuki and Abe[33] with a subsequent search for a minimum rectangular enclosing area,[34] as shown in Figure 5C and Figure 5D. By identifying three corresponding corners in the two different images, the projection matrix to transform from the laser scanner coordinate system to the camera coordinate system (see Equation (2)) can eventually be determined and is given by

$$\mathbf{T}_{\text{affine}} = \begin{pmatrix} 2.5583 & -0.0321 & 253.27 \\ 0.0424 & 2.7456 & -523.44 \end{pmatrix} \tag{3}$$

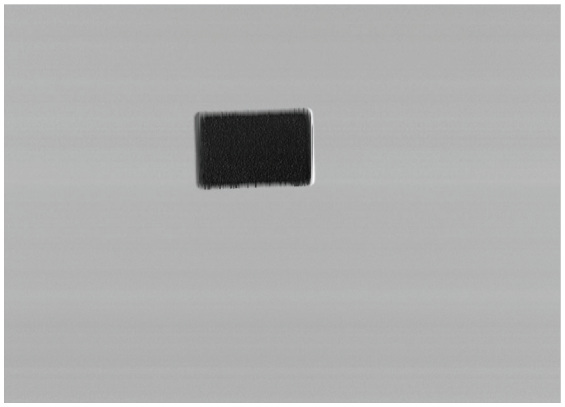

(A) Gray-scale image of the laser-scanner profile data obtained for the rectangular calibration target

(B) Monochrome camera image of the rectangular calibration target

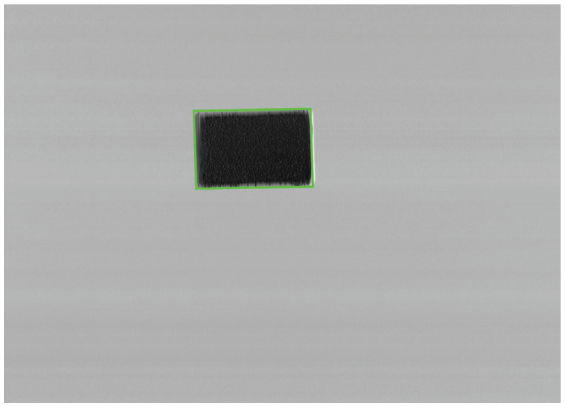

(C) Contour detection of the calibration target from the laser-scanner profile data. The green rectangle represents the minimum enclosing area.

(D) Contour detection of the imaged calibration target. The green rectangle represents the minimum enclosing area.

FIGURE 5 Illustration of the sensor data fusion process to match laser scanner and camera data using a rectangular calibration target. Assuming affinity, the transformation from one coordinate system into the other, and therefore the matching procedure, can be described by a translation, dilation, and rotation, which can be summarized in a simple projection matrix. To determine this matrix, corresponding data points in the image representations (upper row) of both data acquisition systems are identified by means of object recognition (lower row)

for the current experimental setup. As long as the geometry between the laser scanner and the camera is not changed in the experimental setup, $\mathbf{T}_{\text{affine}}$ can automatically be applied right after each data acquisition run. The resulting depth profile for an arbitrary test object is then stored together with the captured image data as a new structure which, in the discussed microsurgical application, enables the direct access of depth and distance information at each given pixel location.

This, however, is only feasible as long as there are no perturbations in the acquired data of the laser scanner so that a pixelwise mapping can be performed. In general, laser triangulation works best on diffusely reflecting, nonspecular surfaces, where the incident laser beam is scattered such that a significant amount of scattered light is received by the PSD. In real-world measurements certain functional impairments, like, for example, specular reflections and occlusions, cannot be precluded entirely and, as a result, lead to missing data points in the laser scan matrix vitiating not just the mapping process but also reducing the visualization quality of the captured depth profiles.

To deal with these perturbations and to minimize the impact of missing data points, interpolation based on a radial basis function (RBF) approach should be applied. In general, RBF methods are used to approximate multivariate functions that are only known at a finite number of points by linear combinations of terms based on a single univariate, radially symmetric function. Here, we use them to interpolate missing data points in the laser scan matrix from their known surrounding measurement values and to approximate the test object's surface for visualization purposes.

Assume that the surface can be described by a smooth function $f : \mathbb{R}^2 \to \mathbb{R}$, where n function values

$$f(\mathbf{x}_i) = y_i, \quad \text{for } i = 1, \dots, n, \tag{4}$$

are known by measurement. This, in general, unknown function can then be approximated by

$$s(\mathbf{x}) = \sum_{i=1}^{n} \lambda_i \varphi(||\mathbf{x} - \mathbf{x}_i||), \tag{5}$$

which eventually allows for a depth measure evaluation at any given point **x.** Here, $\varphi(r)$ is the adopted RBF, which is a radially symmetric, real-valued function defined on $[0, \text{inf})$, $\mathbf{x}_i$ are the data points for which the function value y_i is known, λ_i are scalar parameters, and $||\cdot||$ denotes a suitably chosen norm, usually (and also in the present case) the Euclidean norm$|\cdot|$.

As discussed by Carr et al,[35] a simple linear RBF $\varphi(r) = r$ is a good choice for reconstructing surface data and should therefore be used in the following. Hence, Equation (5) simplifies to

$$s(\mathbf{x}) = \sum_{i=1}^{n} \lambda_i |\mathbf{x} - \mathbf{x}_i|. \tag{6}$$

Given that

$$s(\mathbf{x}_i) = f(\mathbf{x}_i) = y_i, \quad \text{for } i = 1, \dots, n, \tag{7}$$

a $n \times n$ linear system of equations (LSE) can eventually be derived to solve for the coefficients λ_i that specify the RBF in Equation (6). This LSE is given by

$$\mathbf{A}\boldsymbol{\lambda} = \mathbf{y}, \tag{8}$$

where $\boldsymbol{\lambda} = (\lambda_1, \lambda_2, \dots, \lambda_n)^{\mathsf{T}}$ summarizes the RBF coefficients and $\mathbf{y} = (y_1, y_2, \dots, y_n)^{\mathsf{T}}$ represents the known (measured) surface values. The entries of the square-symmetric interpolation matrix **A** are then given by

$$A_{ij} = |\mathbf{x}_i - \mathbf{x}_j|, \quad \text{with } i,j = 1, \dots, n, \tag{9}$$

which is nonsingular and, consequently, guarantees the unique existence of the coefficients λ_i as long as the chosen RBF $\varphi(r)$ is strictly positive definite,[36] which, using a simple linear RBF in conjunction with the Euclidean norm, is the case here.

By solving the LSE of Equation (8), one obtains the coefficient vector $\boldsymbol{\lambda}$ and, thus, the surface approximation function $s(\mathbf{x})$ of Equation (6), which can subsequently be used for visualization and sensor data fusion, as will be shown in the

following section. In each case, a Python implementation of the LAPACK driver routine sSYSV[37] was used. It is based on the diagonal pivoting method with a partial pivoting strategy introduced by Bunch and Kaufmann[38] and allows for finding the corresponding solution of the symmetric LSE in a very efficient manner.

3.3 | Results for organic tissue samples

As a first proof-of-concept of the proposed method for high-resolution depth measurements in microsurgery based on laser triangulation, results obtained for two different organic tissue samples, that is, a piece of fractured bone from a pig's femur and muscle tissue from the upper part of a pig's shoulder, are reported in this section. Figures 6 and 7 visualize the respective measurement and sensor data fusion outcomes. The corresponding raw and RBF data can be downloaded via our institutional webpage.[39] This source also provides further access to the results of some additional tissue samples (webpage-only) which, for the sake of brevity and due to similar conclusions to be drawn, are not explicitly discussed here.

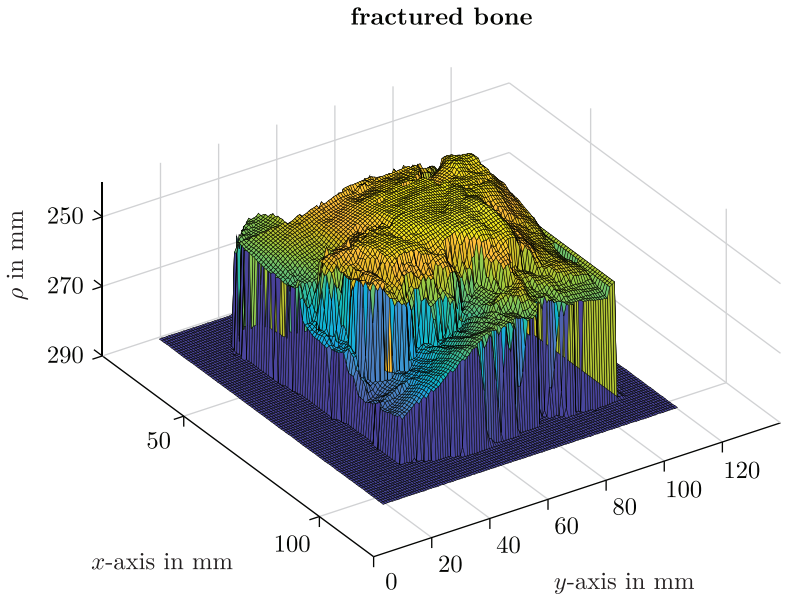

(A) Three-dimensional depth reconstruction of the fractured bone sample. The RBF method was applied for the interpolation of missing data points.

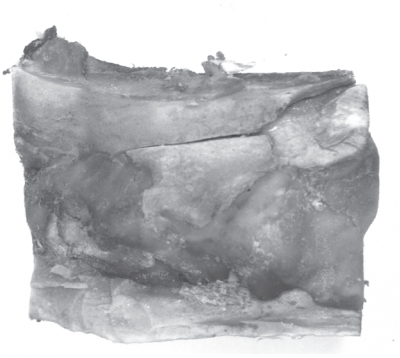

(B) Gray-scale image of the fractured bone sample as acquired by the monochrome image capturing system

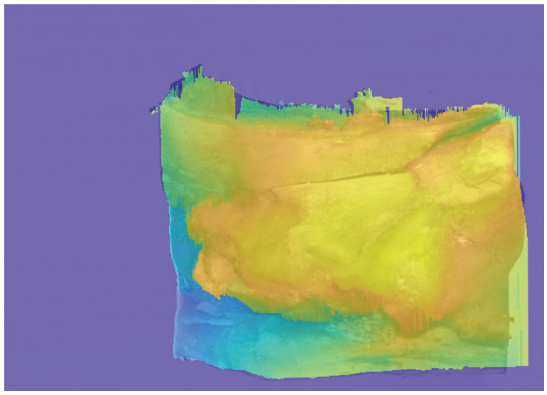

(C) Color map overlay to visualize the sensor data fusion process for the fractured bone sample

FIGURE 6 Visual representation of the laser-triangulation depth measurement results for the fractured bone sample. The fusion of laser scanner and camera data eventually yields a data matrix containing both image and depth information at each given pixel location

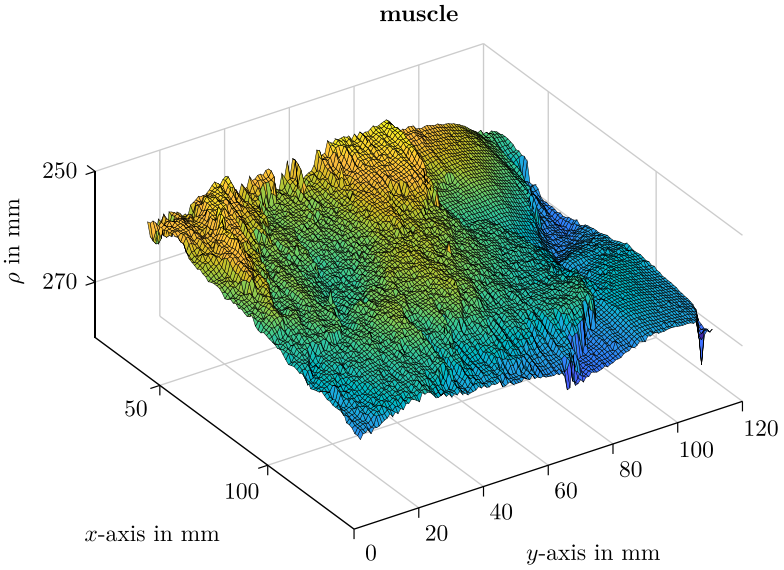

(A) Three-dimensional depth reconstruction of the muscle tissue sample. The RBF method was applied for the interpolation of missing data points.

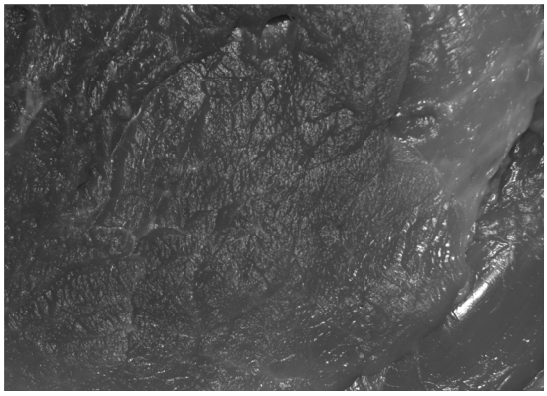

(B) Gray-scale image of the muscle tissue sample as acquired by the monochrome image capturing system

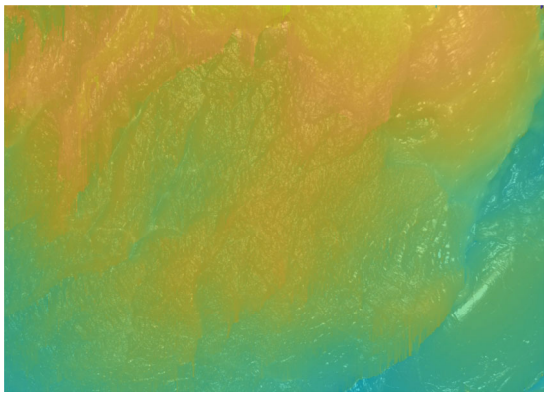

(C) Color map overlay to visualize the sensor data fusion process for the muscle tissue sample

FIGURE 7 Visual representation of the laser-triangulation depth measurement results for the muscle tissue sample. The fusion of laser scanner and camera data eventually yields a data matrix containing both image and depth information at each given pixel location

In all cases—including the webpage-only samples—the proposed method works quite well. It does not only allow for a high-resolution depth map visualization of the respective tissue structures illustrated as three-dimensional surface plots but, based on the applied sensor data fusion, also enables the accurate, pixelwise determination of distance values in order to determine the pixel-dependent scaling factor $\delta^{(i,j)}$ that is required for reflectance estimation and subsequent tissue recognition as outlined in the Introduction section of this article. Problems of incorrect data representations because of failed RBF interpolation are only observed at the edges of the tissue samples, where the corresponding surface gradient becomes overly steep so that the scattered light is not reflected back onto the PSD of the laser scanner. As a result, this yields too large areas of missing data points along the edges. Another source of such functional impairments compromising the RBF processing are occlusions of lower lying tissue layers at the edge structures due to the finite opening angle of the line segment emitted by the laser scanner.

Besides these small, edge-related disturbances, no further severe measurement errors are observed. Comparing, for example, the results obtained for bone and muscle tissue shown in Figures 6 and 7, respectively, an equally good performance of the proposed method can be concluded when assessing the inner structure of the tissue surfaces, that is, all parts

that are sufficiently far from the samples' edges. As can be seen, the tissue fine structures are resolved properly in both cases without showing any nonsmooth perturbations neither at the transitions from osseous to marrow structures in case of the fractured bone sample nor at the transition from fiber to adipose or conjunctive components in case of the muscle tissue. This basically indicates that neither residual surface moisture nor a specific tissue color prevent the proposed method from providing accurate depth measurements when being applied to different kinds of organic tissue samples.

Failures in the data acquisition and/or RBF interpolation of the samples' inner parts are therefore only expected if the tissue itself absorbs to much of the incident light from the laser scanner or prevents the light from being scattered diffusely back into the PSD unit because of the occurrence of too much specular reflections in conjunction with an unfavorable incident angle. In either case, missing data points in the laser scanner data matrix representing these surface areas would be the consequence. As long as these areas are relatively small, the missing data can still be compensated appropriately by the implemented RBF approach. Thus, larger errors or pronounced perturbations were not observed for any of the various organic tissue samples considered in this work. It can therefore be concluded that both absorption and specular reflection seem to be minor issues and little to worry about in practice—at least with regard to the current experimental setup.

4 | CONCLUSION AND OUTLOOK

The exact knowledge of the tissue topology including the option of performing precise three-dimensional distance and contour measurements can facilitate and support the surgeon's workflow within the framework of computer-assisted or AR-guided microsurgical treatments. For example, it may help to choose the appropriate size of patient-tailored implants and prostheses and allow for accurate real-time tracking of instrument tips in order to reduce the risk of complications caused by harmful tissue contact.[5,6]

In the current article, however, a slightly different use case was sketched for research motivation. As part of a previous exploratory study on automated tissue recognition in digital stereoscopic microsurgery based on Wiener-filter reflectance estimation from HSI input, it has been shown that the distance and angle of the captured tissue surface with respect to the illumination and image capturing modules of the microscope must be determined with high accuracy in order to achieve a sufficiently good tissue recognition performance. In this context, a depth accuracy of less than ± 0.3 mm has been concluded to be favorable for application. Based on the assumption of typical microscope specifications and the benchmark results of high-performance stereomatching algorithms usually applied for such tasks, it has been demonstrated that the naïve approach of using the microscope's stereoscopic image data for directly extracting depth information seems to be inappropriate to comply with these accuracy requirements.

In this work, a new method for high-resolution depth measurements in digital microsurgical applications was therefore proposed adopting the principle of laser triangulation. With the experimental setup discussed in Section 2, the expected error in depth measurements performed on a dedicated reference target was shown to be of the order of ± 104 μm, which conforms to the required depth resolution of at least ± 0.3 mm or better. Given that the proposed laser-triangulation method clearly complies with these requirements, a method of sensor data fusion was subsequently discussed in order to properly match the laser scanner and camera data in a straightforward and intuitive manner. In this context, a strategy based on RBF interpolation techniques was introduced to handle missing or corrupt data as an integral part of this automated mapping process. The proposed method was eventually used to acquire high-resolution depth profiles of various organic tissue samples. It could be shown that, besides some small disturbances at the samples' edges, excellent measurement performance was achieved for all considered tissue structures without observing any larger errors or pronounced perturbations. Thus, it was concluded that, with regard to the current experimental setup, failures in the data acquisition and RBF interpolation are only expected if the tissue itself absorbs to much of the incident light or prevents the light from being scattered diffusely back into the PSD unit because of an unfavorable combination of specular reflections and a too large incident angle. In all other cases, the system performs sufficiently well to provide high-resolution depth measurements that comply with the requirements to be used for subsequent Wiener-filter reflectance estimation or any other microsurgical treatment that requires accurate depth and distance measurements.

So far, the current setup is quite experimental and may serve only as a first proof-of-concept. Thus, based on the encouraging results reported in this work, the next logical step would be to proceed with the system integration into a real digital stereoscopic microsurgical device. The aim of this step is to combine the sensor data of the laser scanner with the stereoscopic image data of the microscope in a similar manner performed here on two-dimensional image data. The expected

benefit of such a system integration is that the additional availability of native stereoscopic information from the microscope may help to improve the RBF performance and to deal with missing data of the laser scanner at edge-like structures in the surgical field. In these critical regions, depth information reconstructed from the microscopes stereoscopic image data, even though less accurate, can be used to fill the voids in the corresponding data matrix for achieving a more accurate RBF interpolation showing less pronounced perturbations at the tissue edges. Potential bottlenecks of such a system integration can be identified in the obviously more complex calibration requirements due to the use of mostly sophisticated zoom lens designs and the constraints typically related to microscopic applications, such as, for example, a small depth-of-field and steep viewing angles complicating the camera-laser registration. With the focus of the current setup being on the accuracy evaluation of the laser-triangulation approach, these other challenges have not been addressed yet, but must be considered as part of future developments. Besides, it remains an open question how exactly the scanning process along the *y*-axis can be implemented when integrating the laser device into a microscope's head.

In addition, more sophisticated interpolation algorithms should also be tested, not only for overall interpolation performance but also for computational speed with regard to an intended real-time implementation. For a quantitative performance evaluation under real microscopic conditions, it is further necessary to know the ground truth of the tissues' surface structures used for testing. However, organic tissue seems inappropriate for this purpose. With recent breakthroughs in 3D-printing techniques,[40-42] models of known geometry and similar optical properties as their organic counterparts might be an adequate solution to become an integral part of these future research intentions.

ACKNOWLEDGEMENTS

The authors would like to thank the Micro-Epsilon Messtechnik GmbH & Co. KG for providing the two laser-triangulation devices and their very appreciated support regarding all issues of data acquisition and device control. Special thanks go to Dr-Ing Armin Schneider from the ARRI Medical GmbH for fruitful discussions on digital microsurgery. The authors received no specific funding for this work. Open access funding enabled and organized by Projekt DEAL.

PEER REVIEW INFORMATION

Engineering Reports thanks the anonymous reviewers for their contribution to the peer review of this work.

CONFLICT OF INTEREST

The authors declare that there were no conflicts of interest related to this article.

DATA AVAILABILITY STATEMENT

Supplementary material associated with this article can be found online at url: https://www.lichttechnik.tu-darmstadt.de/forschung_lt/daten_zu_wissenschaftl___veroeffentlichungen/inhalt_mit_marginalienspalte_71.de.jsp. The data that support the reported findings are openly available and can also be downloaded from this source.

ORCID

Sebastian Babilon https://orcid.org/0000-0001-8002-1220
Paul Myland https://orcid.org/0000-0002-5654-837X
Julian Klabes https://orcid.org/0000-0001-8725-3163

REFERENCES

1. Franklin AJ, Sarangapani R, Yin L, Tripathi B, Riemann C. Digital vs analog surgical visualization for vitreoretinal surgery. *Retinal Phys*. 2017;14(May):34–36-38–40.
2. Samy RN. Adoption of new technology. *Curr Opin Otolaryngol Head Neck Surg*. 2016;24(5):381.
3. Mayer HM, ed. *Minimally Invasive Spine Surgery: A Surgical Manual*. New York, NY: Springer-Verlag; 2006.
4. Herlan S, Marquardt JS, Hirt B, Tatagiba M, Ebner FH. 3D exoscope system in neurosurgery–comparison of a standard operating microscope with a new 3d exoscope in the cadaver lab. *Operat Neurosurg*. 2019;17(5):518-524.
5. Gard N, Rosenthal JC, Jurk S, Schneider A, Eisert P. Image-based measurement by instrument tip tracking for tympanoplasty using digital surgical microscopy. Paper presented at: Proceedings of the SPIE 10951, Medical Imaging 2019: Image-Guided Procedures, Robotic Interventions, and Modeling. The International Society for Optics and Photonics (SPIE); 2019:1095119; San Diego, CA.
6. Wisotzky EL, Rosenthal JC, Eisert P, et al. Interactive and multimodel-based augmented reality for remote assistance using a digital surgical microscope. Paper presented at: Proceedings of the 26th IEEE Conference on Virtual Reality and 3D User Interfaces; 2019:1477-1484; Osaka, Japan.

7. Aschke M, Wirtz CR, Raczkowsky J, Wörn H, Kunze S. Augmented reality in operating microscopes for neurosurgical interventions. Paper presented at: Proceedings of the 1st International IEEE EMBS Conference on Neural Engineering; 2003652-655; Capri Island, Italy.
8. Khor WS, Baker B, Amin K, Chan A, Patel K, Wong J. Augmented and virtual reality in surgery–The digital surgical environment: applications, limitations and legal pitfalls. *Ann Transl Medic*. 2016;4(23):454.
9. Lu G, Fei B. Medical hyperspectral imaging: a review. *J Biomed Opt*. 2014;19(1):10901.
10. Wisotzky EL, Arens P, Uecker FC, Hilsmann A, Eisert P. A hyperspectral method to analyze optical tissue characteristics *in vivo*. *Int J Comput Assist Radiol Surg*. 2018;13(Suppl 1):46-47.
11. Wisotzky EL, Uecker FC, Arens P, Dommerich S, Hilsmann A, Eisert P. Intraoperative hyperspectral determination of human tissue properties. *J Biomed Opt*. 2018;23(9):091409.
12. Wisotzky EL, Kossack B, Uecker FC, et al. Validation of two techniques for intraoperative hyperspectral human tissue determination. Paper presented at: Proceedings of SPIE 10951, Medical Imaging 2019: Image-Guided Procedures, Robotic Interventions, and Modeling. The International Society for Optics and Photonics (SPIE); 2019:109511Z; San Diego, CA.
13. Babilon S, Myland P, Klabes J, Simon J, Khanh TQ. Spectral reflectance estimation of organic tissue for improved color correction of video-assisted surgery. *J Electron Imag*. 2018;27(5):053012.
14. Stigell P, Miyata K, Hauta-Kasari M. Wiener estimation method in estimating of spectral reflectance from RGB images. *Pattern Recognit Image Anal*. 2007;17(2):233-242.
15. Haneishi H, Hasegawa T, Hosoi A, Yokoyama Y, Tsumura N, Miyake Y. System design for accurately estimating the spectral reflectance of art paintings. *Appl Opt*. 2000;39(35):6621-6632.
16. Shimano N, Terai K, Hironaga M. Recovery of spectral reflectances of objects being imaged by multispectral cameras. *J Opt Soc Am A*. 2007;24(10):3211-3219.
17. Urban P, Rosen MR, Berns RS. A spatially adaptive wiener filter for reflectance estimation. Paper presented at: Proceedings of the 16th Color and Imaging Conference. Society for Imaging Science and Technology (IS&T); 2008:279-284; Portland, OR.
18. Urban P, Rosen MR, Berns RS. Spectral image reconstruction using an edge preserving spatio-spectral Wiener estimation. *J Opt Soc Am A*. 2009;26(8):1865-1875.
19. van Ginneken B, Kerkstra S, Meakin J. Stereo correspondence and reconstruction of endoscopic data sub-challenge; 2020. https://endovissub2019-scared.grand-challenge.org/. Accessed September 28, 2020.
20. Mansour M, Davidson P, Stepanov O, Piché R. Relative importance of binocular disparity and motion parallax for depth estimation: a computer vision approach. *Remote Sens*. 2019;11(17):1990.
21. Gallup D, Frahm J, Mordohai P, Pollefeys M. Variable baseline/resolution stereo. Paper presented at: Proceedings of the 2008 IEEE Conference on Computer Vision and Pattern Recognition; 2008:1-8; Anchorage, AK, IEEE.
22. Scharstein D, Szeliski R, Hirschmüller H. Middlebury stereo evaluation – version 3. http://vision.middlebury.edu/stereo/eval3/. Accessed September 29, 2020.
23. Niazi ZBM, Essex TJH, Papini R, Scott D, McLean NR, Black MJM. New laser doppler scanner, a valuable adjunct in burn depth assessment. *Burns*. 1993;19(6):485-489.
24. Ireland AJ, McNamara C, Clover MJ, et al. 3D Surface imaging in dentistry – what we are looking at. *Br Dent J*. 2008;205(7):387-392.
25. Chromy A, Zalud L. Robotic 3D scanner as an alternative to standard modalities of medical imaging. *Springerplus*. 2014;3:13.
26. Micro-epsilon messtechnik GmbH & Co. KG scanCONTROL // 2D/3D laser scanners (laser profile sensors); 2020. https://www.micro-epsilon.com/download/products/cat-scancontrol/dax--scanCONTROL-29x0--en.html#page=2&zoom=Fit. Accessed September 29, 2020.
27. IDS imaging development systems GmbH . Datenblatt UI-5490SE-M-GL Rev.2. https://de.ids-imaging.com/IDS/datasheet_pdf.php?sku=AB.0010.1.52802.23. Accessed September 29, 2020.
28. Xu D, Jiang Y. A method and implementation of fully digitized continuous microstep for step motor. Paper presented at: Proceedings of the 1997 IEEE International Electric Machines and Drives Conference; 1997:TC2/9.1–TC2/9.3; Milwaukee, WI, IEEE.
29. Watanabe K, Yokote H. A microstep controller of a DC servomotor. *IEEE Trans Instrum Meas*. 1990;39(6):867-869.
30. Yang Z, Cohen FS. Image registration and object recognition using affine invariants and convex hulls. *IEEE Trans Image Process*. 1999;8(7):934-946.
31. Chan FY, Lam FK, Zhu H. Adaptive thresholding by variational method. *IEEE Trans Image Process*. 1998;7(3):468-473.
32. Kamel M, Zhao A. Extraction of binary character/graphics images from grayscale document images. *CVGIP Graph Models Image Process*. 1993;55(3):203-217.
33. Suzuki S, Abe K. Topological structural analysis of digitized binary images by border following. *Comput Vis Graph Image Process*. 1985;30(1):32-46.
34. Toussaint GT. Solving geometric problems with the rotating calipers. Paper presented at: Proceedings of the IEEE Mediterranean Eletrotechnical Conference; 1983:A10.02/1–4; Athens, Greece, IEEE.
35. Carr JC, Beatson RK, Cherrie JB, et al. Reconstruction and representation of 3D objects with radial basis functions. Paper presented at: Proceedings of the 28th Annual Conference on Computer Graphics and Interactive Techniques. Association for Computing Machinery; 2001:67-76; New York, NY.
36. Micchelli CA. Interpolation of scattered data: distance matrices and conditionally positive definite functions. *Constr Approx*. 1986;2:11-22.
37. Higham NJ. Stability of the diagonal pivoting method with partial pivoting. *SIAM J Matrix Anal Appl*. 1997;18(1):52-65.
38. Bunch JR, Kaufman L. Some stable methods for calculating inertia and solving symmetric linear systems. *Math Comput*. 1977;31(137):163-179.

39. Babilon S. Raw data of the depth measurements performed on real organic tissue samples; 2020. https://www.lichttechnik.tu-darmstadt.de/forschung_lt/daten_zu_wissenschaftl___veroeffentlichungen/inhalt_mit_marginalienspalte_71.de.jsp. Accessed September 29, 2020.
40. Tack P, Victor J, Gemmel P, Annemans L. 3D-printing techniques in a medical setting: a systematic literature review. *Biomed Eng Online*. 2016;15:115.
41. Lenzen-Schulte M. Anatomische Rekonstruktion – 3-D-Drucker erobern den OP-Saal. *Deutsches Ärzteblatt*. 2017;114(38):1704-1707.
42. Brunton A, Arikan CA, Tanksale TM, Urban P. 3D printing spatially varying color and translucency. *ACM Trans Graph*. 2018;37(4):157.

How to cite this article: Babilon S, Myland P, Schlestein L, Klabes J, Khanh TQ. High-resolution depth measurements in digital microscopic surgery. *Engineering Reports*. 2020;e12311. https://doi.org/10.1002/eng2.12311